Characterization of Pd/Y multilayers with B₄C barrier layers using GIXR and X-ray standing wave enhanced HAXPES

M.-Y. Wu,[a] Q.-S. Huang,[b]* K. Le Guen,[a] V. Ilakovac,[a,c] B.-X. Li,[a,d] Z.-S. Wang,[b] A. Giglia,[e] J.-P. Rueff[a,f] and P. Jonnard[a]*

[a]Laboratoire de Chimie Physique – Matière et Rayonnement, Sorbonne University, UMR CNRS 7614, 4 Place Jussieu, 75005 Paris, France, [b]Key Laboratory of Advanced Micro-Structured Materials MOE, Institute of Precision Optical Engineering, School of Physics Science and Engineering, Tongji University, Shanghai 200092, People's Republic of China, [c]Université de Cergy-Pontoise, F-95031 Cergy-Pontoise, France, [d]Northwestern Polytechnical University, 710072 Xi'an, People's Republic of China, [e]CNR, Istituto Officina Materiali, 34149 Trieste, Italy, and [f]Synchrotron SOLEIL, L'Orme des Merisiers, BP 48, Saint-Aubin, 91192 Gif-sur-Yvette Cedex, France. *Correspondence e-mail: huangqs@tongji.edu.cn, philippe.jonnard@upmc.fr

Pd/Y multilayers are high-reflectance mirrors designed to work in the 7.5–11 nm wavelength range. Samples, prepared by magnetron sputtering, are deposited with or without B₄C barrier layers located at the interfaces of the Pd and Y layers to reduce interdiffusion, which is expected from calculating the mixing enthalpy of Pd and Y. Grazing-incident X-ray reflectometry is used to characterize these multilayers. B₄C barrier layers are found to be effective in reducing Pd–Y interdiffusion. Details of the composition of the multilayers are revealed by hard X-ray photoemission spectroscopy with X-ray standing wave effects. This consists of measuring the photoemission intensity from the samples by performing an angular scan in the region corresponding to the multilayer period and an incident photon energy according to Bragg's law. The experimental results indicate that Pd does not chemically react with B nor C at the Pd–B₄C interface while Y does react at the Y–B₄C interface. The formation of Y–B or Y–C chemical compounds could be the reason why the interfaces are stabilized. By comparing the experimentally obtained angular variation of the characteristic photoemission with theoretical calculations, the depth distribution of each component element can be interpreted.

1. Introduction

Periodic multilayer mirrors are important optical components that are applied in the X-ray and extreme ultraviolet spectra ranges. Understanding the relation between the structures of multilayer optics and their optical properties is crucial for their design. Exploration of the structures of the multilayers by multiple analyzing methods, such as reflectance and photoemission measurements, helps to improve the deposition process and eventually the optical performance.

The Pd/Y multilayer was first proposed and studied by Montcalm *et al.* (1996). Such a material combination is promising as simulation gives up to 65% reflectance of such a design for radiation of 9.5 nm wavelength. The potential applications vary from EUV spectroscopy and plasma diagnosis to synchrotron radiation or free-electron laser instruments. A crucial factor that may compromise the performance of the mirror is the interdiffusion of Pd and Y. Nitridation of the Pd/Y multilayer by introducing nitrogen during the deposition process can reduce the interdiffusion (Xu *et al.*, 2015; Wu *et al.*, 2017*a*), yet the nitridated multilayers suffer a
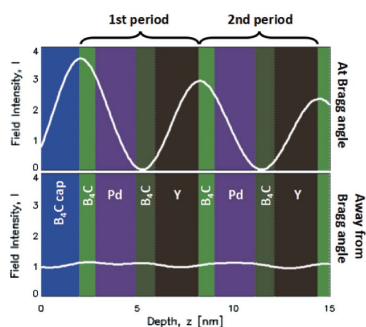
reflectance loss. The optical performance of the mirror is thus lower than expected from theoretical calculations. The insertion of a B_4C barrier layer at the interface has been reported by Windt & Gullikson (2015) as another effective means to obtain smoother interfaces and thus improve the optical performance of the Pd/Y system.

In this paper we focus on Pd/Y multilayers inserted with B_4C barrier layers in an attempt to find out more details about the mechanism of how the barrier layers reduce the interdiffusion. We report the characterization of the samples using grazing-incident X-ray reflectometry (GIXR) and X-ray standing wave enhanced hard X-ray photoelectron spectroscopy (HAXPES). The experimental performances of Pd/Y multilayer mirrors are found to be far worse from the simulations. This could be explained by many factors such as interface roughness and Pd–Y interdiffusion. We begin to find reasons for the interdiffusion by performing mixing enthalpy calculations.

HAXPES (Fadley, 2013, 2016) provides a much higher value for the probed depth compared with conventional X-ray photoelectron spectroscopy, thanks to the long inelastic mean free path (IMFP) of the emitted electrons due to their high kinetic energy. Thus HAXPES is suitable for analysing a considerable part of the structure buried under the surface. The disadvantage, *i.e.* the low efficiency due to the high energy of the incident photons which leads to a low ionization cross section, can be counterbalanced by using a high-brilliance synchrotron radiation light source. X-ray standing waves (XSW), which appear as a quasi-sinusoidal periodic electric field perpendicular to the surface of the multilayer, are generated by the interference between the incident photon beam and that reflected by the irradiated multilayer (Bartel *et al.*, 2005). A depth distribution of the electric field intensity in the multilayer results in a depth distribution of the ionization rate. Such a distribution can be modulated by varying the grazing-incident angle of the photon beam. The effect can be observed by measuring related phenomena such as characteristic X-ray emission (Wu *et al.*, 2017b; Tu *et al.*, 2015) and photoemission (Giglia *et al.*, 2013) as a function of incident angle. The combination of HAXPES and XSW offers the unique advantage of a non-destructive characterization method with which detailed information about the multilayer structure can be obtained, such as the chemical compounds formed at the interface.

2. Theoretical and experimental methods

The mixing enthalpy calculated following the Miedema model (Miedema *et al.*, 1980) indicates that intermixing is possible between the Pd and Y layers. The Pd–Y binary phase diagram (Kardellass *et al.*, 2013) also shows that multiple possible compounds may form. Unfortunately the constants for the calculations concerning B_4C are not available in the literature to our knowledge, and thus the intermixing of Pd–B_4C and Y–B_4C cannot be predicted using the mixing enthalpy. However, the enthalpy of formation ΔH_f of palladium as well as yttrium borides and carbides is available in the literature (Montcalm *et*

al., 1996; Meschel & Kleppa, 2001). For B_4C/Pd, the enthalpy of formation is positive, indicating a low probability of the formation of the chemical compound. However, for Y, ΔH_f of YB_2, YB_4, Y_2C and Y_2C_3 are -36, -52, -32 and -51 kJ mol^{-1}, respectively. Chemical reactions of Y–B and Y–C are thus expected. Yet seen these values of the enthalpy of formation, it is difficult to distinguish YB_2 from Y_2C (and YB_4 from Y_2C_3), thus the chemical selectivity of the reactions (Y–B or Y–C) cannot be predicted. ΔH_f of Y/Pd is found to be -94 kJ mol^{-1} as further evidence of the Pd–Y interdiffusion, in agreement with our calculation of mixing enthalpy with different Pd–Y mole fractions.

A series of Pd/Y-based samples are deposited using the DC magnetron sputtering technique. The original design for the mirror is Pd/Y repeating 40 times and deposited on sliced and polished Si (100) wafers with a 4 nm period thickness (2 nm Pd and 2 nm Y). A 2.5 nm B_4C capping layer is deposited on top of the sample to prevent the oxidation of the component metals. Three other samples are prepared: 1 nm-thick B_4C barrier layers are inserted at either interface of these two metals or even both interfaces to prevent the interdiffusion of the two metals. Thus the new structures of the samples are B_4C/Pd/Y (1/2/2 nm), Pd/B_4C/Y (2/1/2 nm) and B_4C/Pd/B_4C/Y (1/2/1/2 nm). Here, the order of the layers is given from the top to the bottom of the stack, so B_4C/Pd/Y means B_4C-on-Pd, then Pd-on-Y, Y-on-B_4C and so on. Considering the X-ray attenuation and the IMFP of the emitted photoelectrons, we grew only 20-period structures for the last sample, whose period is thicker than the others, instead of the standard 40-period original structures.

Each sample is characterized by GIXR using Cu $K\alpha$ radiation (8048 eV). The structure is determined by fitting the GIXR result using the software *IMD* (Windt, 1998). The parameters of this structure are then introduced into the software *YXRO* (Yang *et al.*, 2013) in order to anticipate the X-ray standing wave field forming inside the stack and the HAXPES result.

HAXPES measurements were performed at the GALAXIES beamline of the SOLEIL synchrotron facility (Céolin *et al.*, 2013). The incident photon energy was set to 10 keV. With such an energy we can expect an IMFP of 6.4–8.5 nm of the emitted photoelectron depending on the element and the core level. This allows the probed depth, estimated to be three times that of the IMFP, to be approximately equal to 4–5 periods of the multilayer. However, the photoionization cross section is very small for 10 keV photons, for example 6.5×10^{-25} m^2 for the Pd $2p_{3/2}$ core level (Scofield, 1973). This experimental difficulty is overcome by high-flux synchrotron radiation which guarantees good quality data.

The experimental setup is presented in Fig. 1(*a*) where the photon beam impinges onto the sample with the grazing incident angle θ recorded by a goniometer with an angular resolution approximately equal to 0.008°. Calibration of the binding energy of the photoemission spectra is carried out using the Au $4f_{7/2}$ peak which is 84.0 eV. According to the structure of the sample B_4C/Pd/B_4C/Y determined by GIXR,
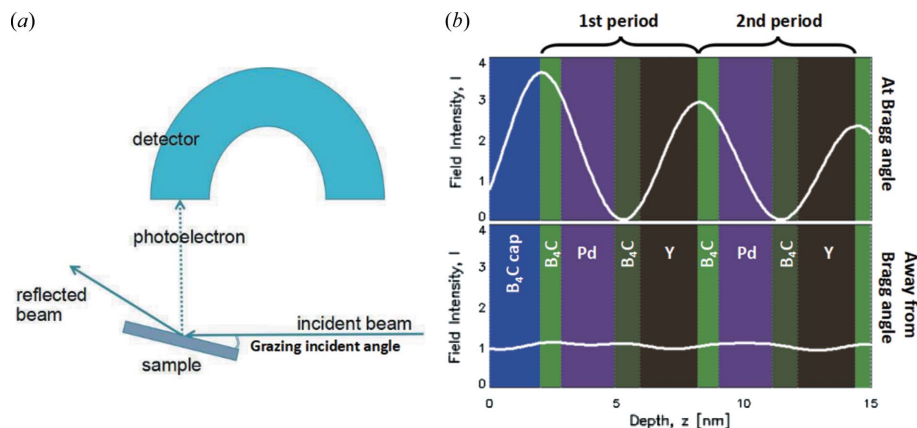
(a)

(b)

Figure 1
(a) Scheme of the experimental setup. (b) Calculation of the depth distribution of the X-ray standing wave electric field within the $B_4C/Pd/B_4C/Y$ multilayer (6.2 nm period), with the incident beam (10 keV) introduced at the first-order Bragg angle (0.63°) and away from the Bragg angle (0.9°).

angle moves away from the Bragg angle (0.9°, for example) due to the loss of reflectance. The electron analyzer is positioned perpendicular to the incident photon beam. Photoemission is recorded while the sample is rotated around the Bragg angle. A variation of the intensity of the photoemission is observed owing to the modulation of the intensity of the X-ray standing wave field.

3. Results and discussion

The experimental and fitted GIXR curves are presented in Fig. 2. The parameters, *i.e.* thickness and interface width of the various layers, of the samples are then extracted from the fitting procedure and are listed in Table 1. To distinguish the samples easily, in the following we use sample numbers as indicated in Table 1. The interface width parameter in this table stands for both the geometrical roughness and the interdiffusion of the materials at the interfaces between the described layer and the previous one. For a Pd/Y multilayer modeled with perfect interfaces (no interface roughness nor interdiffusion), we expect a high reflectance as presented in Fig. 2(a) (dotted line). However, the interdiffusion, as
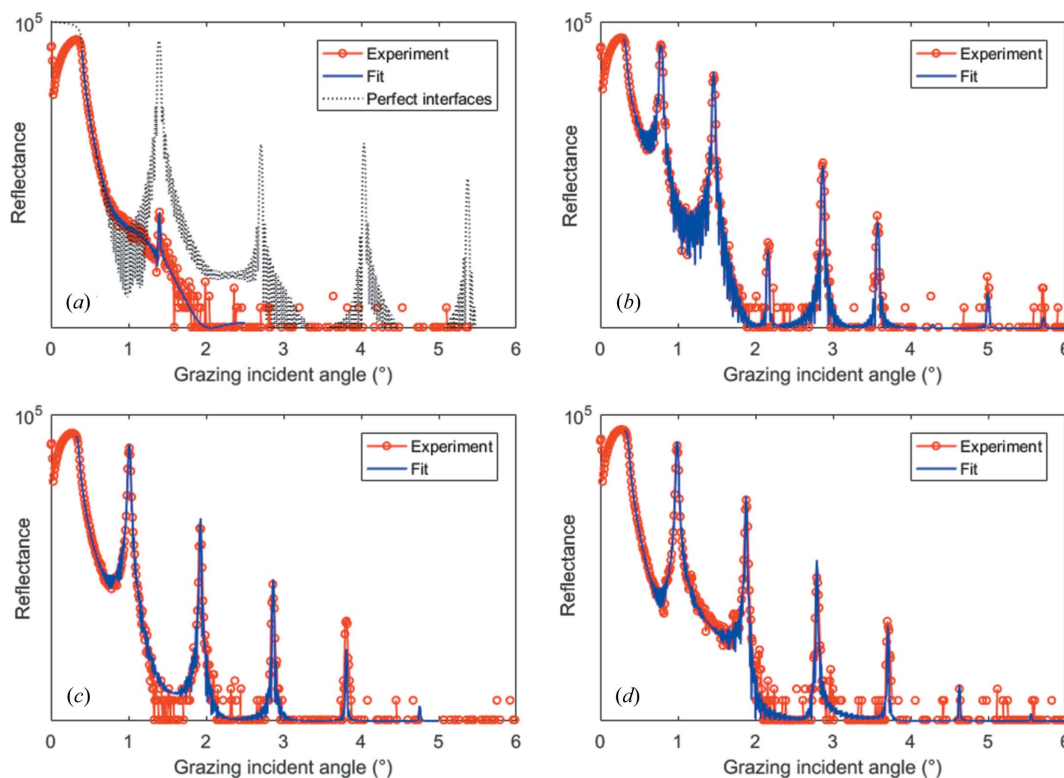
with an incident photon energy of 10 keV a 74% reflectance of the incident radiation can be expected at the first-order Bragg angle. This indicates an intense X-ray standing wave field, leading to a clear depth distribution of the ionization rate as presented in Fig. 1(b) for the $B_4C/Pd/B_4C/Y$ sample where enhanced ionization can be found at the anti-nodal planes of the field while reduced ionization can be found at the nodal planes in the case where the incident angle is set at the Bragg angle (0.63°). The standing wave field fades while the incident

Figure 2
Measured (red dots) and fitted (blue lines) GIXR curves of the multilayers (logarithm scale). (a) Sample 1 (Pd/Y). (b) Sample 2 ($B_4C/Pd/B_4C/Y$). (c) Sample 3 ($B_4C/Pd/Y$). (d) Sample 4 ($Pd/B_4C/Y$). The dotted line in (a) presents the calculated reflectance of the original design without interface roughness or interdiffusion.

Table 1
Designed structures and values of the parameters extracted from the fit of the experimental GIXR curves of the samples.

Sample	Structure	Designed thickness (nm)	Thickness (interface width) (nm) extracted from the fit of GIXR curves
1	$[Pd/Y]_{40}$	2/2	1.87 (1.67) / 1.43 (1.35)
2	$[B_4C/Pd/B_4C/Y]_{20}$	1/2/1/2	0.99 (0.35) / 2.10 (0.26) / 0.83 (0.27) / 2.29 (0.55)
3	$[B_4C/Pd/Y]_{40}$	1/2/2	0.86 (0.34) / 2.30 (0.32) / 1.50 (0.80)
4	$[Pd/B_4C/Y]_{40}$	2/1/2	2.19 (1.23) / 1.02 (0.30) / 1.57 (0.40)

predicted, is so severe that we barely observe the reflectance peak at the first-order Bragg angle even when viewing the curve on a logarithm scale. The value of the interface width is almost as high as the layer thickness itself and the interferential contrast between different layers is almost completely lost. With B_4C layers as barriers, clear reflectance patterns are observed for the other samples as presented in Fig. 2. The interdiffusion is obviously reduced as we can see from Table 1. The fitting results show that the interdiffusion at the Y-on-Pd interfaces (1.23 nm, sample 4) is stronger than that at the Pd-on-Y interfaces (0.80 nm, sample 3).

The angular variations of the B $1s$, Pd $2p_{3/2}$ and Y $2p_{3/2}$ photoemission spectra of the sample $B_4C/Pd/B_4C/Y$ are presented in Figs. 3(a)–3(c). The B $1s$ photoemission spectra are rather noisy due to the much lower ionization cross section compared with those of Pd $2p_{3/2}$ and Y $2p_{3/2}$. The so-called HAXPES–XSW curve of a core-level peak is obtained in the following way: first, for each of the scanned grazing angles the intensity of the core-level peak is integrated; second, this integral is plotted as a function of angle. This is repeated for all the considered core levels and the obtained result is shown in Fig. 3(d). The integration is performed by considering data 25 eV around the maximum of the photoemission peak. This integration range is chosen so that the background far from the maximum is not taken into account, as it may introduce noise to the XSW curves. The integration also takes into account the subtraction of a Shirley background (Shirley, 1972). The photoemission spectra of Pd $3d$ and Y $3d$ core levels are also recorded at the same time but are not presented here because their HAXPES–XSW curves have approximately the same shape as those of the $2p$ core levels and will not provide additional information. There is an minor difference due to the incertitude or acquisition statistics because of the low intensities of the $3d$ core-level peaks but this can be ignored. The C $1s$
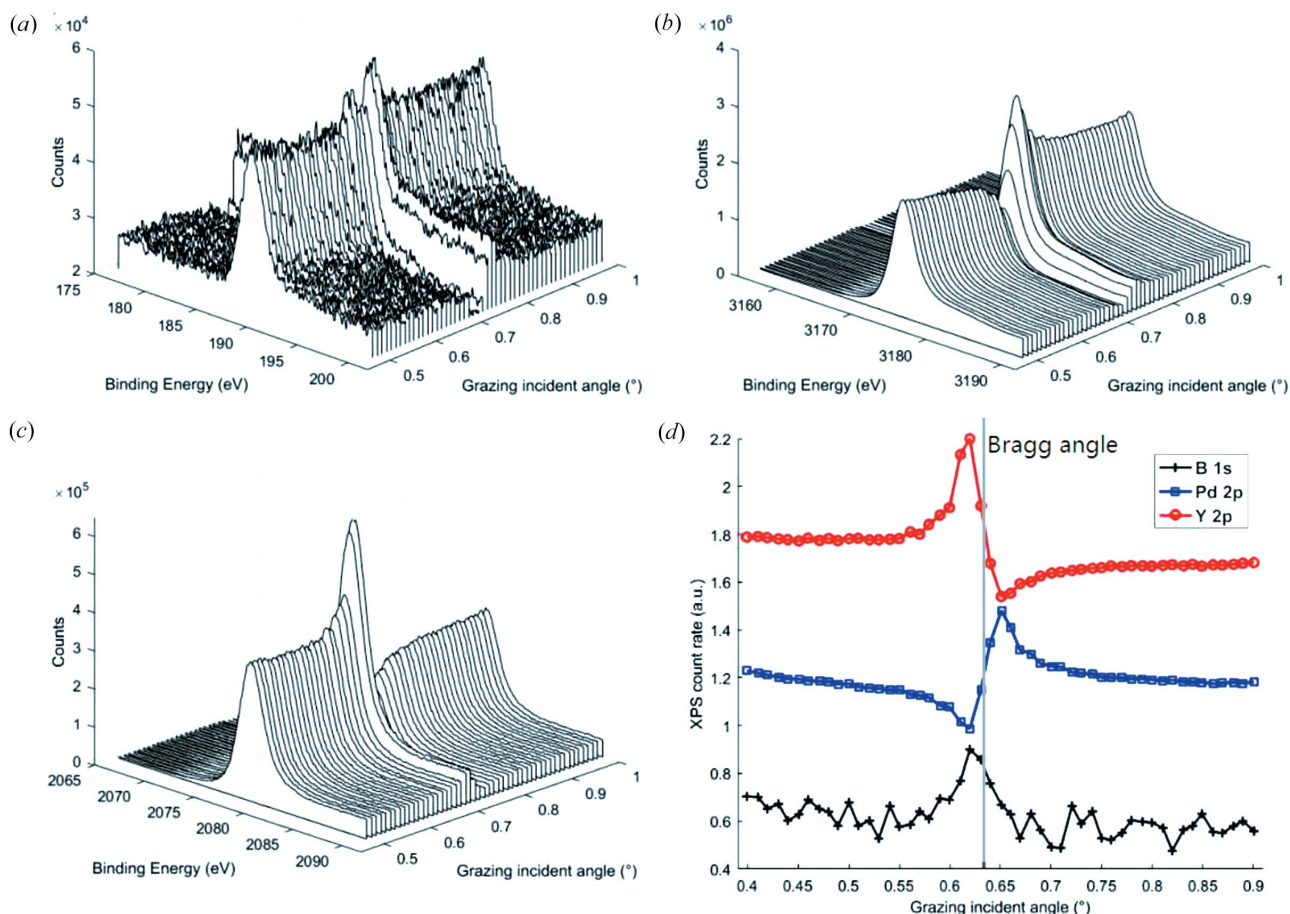

Figure 3
Photoemission spectra of the $B_4C/Pd/B_4C/Y$ multilayer as a function of the grazing incident angle in the vicinity of the Bragg angle (gray solid line) for different core levels. (a) B $1s$, (b) Pd $2p_{3/2}$, (c) Y $2p_{3/2}$, (d) the corresponding HAXPES–XSW curves.
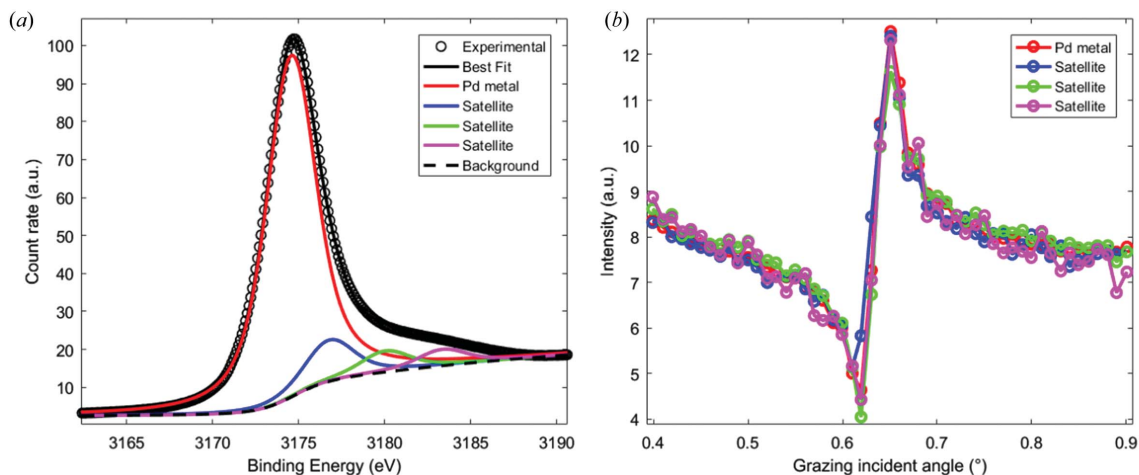
Figure 4
(*a*) Decomposition of the sum of all Pd $2p_{3/2}$ photoemission spectra of sample 2 and (*b*) HAXPES–XSW curves of the corresponding components.

spectra are not presented here owing to surface contamination as the samples are preserved in an atmosphere environment.

The photoemission peaks are decomposed in order to obtain the depth distribution of different chemical states for each element. We are able to retrieve some information from the Pd $2p_{3/2}$ and Y $2p_{3/2}$ spectra whose quality is reliable. Pd $2p_{3/2}$ photoemission spectra of sample 2 are presented in Fig. 4(*a*) where four Voigt peaks are used to fit the experimental curve, which is the sum of the spectra of all angular values in order to gain precision. For the Voigt function, the Gaussian width is 2.00 eV, which is estimated from the bandwidth of the incident photon beam; the Lorentzian width is 2.05 eV, taken from the literature (Campbell & Papp, 2001). The Pd metal peak is found at 3175.2 eV binding energy. We consider other peaks with higher binding energies as satellite peaks, as reported by de Siervo *et al.* (1998). The HAXPES–XSW curve related to each Pd $2p_{3/2}$ component (metal and satellites) is plotted in Fig. 4(*b*). The angular-dependent variations of the intensities of all the satellite peaks are superposed to that of the metal peak, indicating an identical depth distribution. We have considered the possibility that the peak located at 3176.7 eV [blue solid line in Fig. 4(*a*), main contribution beside the Pd metal] belongs to the Pd oxide. However, it is very unlikely that the oxide has the same depth distribution as the Pd metal. Indeed, the deposition of the samples is performed in pure argon. Thus the oxidation of the sample, if it penetrates the 2.5 nm B_4C capping layer and enters into the multilayer, may only occur from the surface. In this case, a pronounced attenuation in the depth distribution would be expected. The observation of an identical depth distribution of each contribution of the photoemission spectrum is evidence for the assumption that the other peaks are but satellites peaks. Since only one chemical state (metal) of Pd is found in the multilayer, the diffusion of the Pd and B_4C layers does not form a new chemical compound (Pd–B or Pd–C). The prediction from the positive enthalpy of formation of B_4C/Pd is confirmed. However, we cannot tell whether Pd and Y form any compound or alloy because, even if they do, the binding energy of the alloy peak would be very close to that

of the metal peak. Given the current energy resolution, it is impossible to distinguish alloy and metal from the HAXPES spectra. The decomposition of Pd $2p_{3/2}$ photoemission spectra of other samples arrives at the same conclusion and thus is not presented here.

Analogous treatment has been carried out for the Y $2p_{3/2}$ core-level peak. The experimental spectrum is best fitted using two Voigt peaks with 2.00 eV Gaussian width and 1.43 eV Lorentzian width (Campbell & Papp, 2001). As presented in Fig. 5(*a*), the major component located at 2078.9 eV in binding energy should be Y metal. The oxidation does not penetrate into the Y layers as previously discussed. The peak which is found at 2081.6 eV stands for the chemical compound of either Y–C or Y–B. To explore the depth distribution of these two chemical states of Y, their HAXPES–XSW curves are depicted for samples 2, 3 and 4 in Figs. 5(*b*), 5(*c*) and 5(*d*), respectively. First we look at the curves of sample 3, $[B_4C/Pd/Y]_{40}$, in Fig. 5(*c*). Compared with Y metal, the HAXPES–XSW curve of the compound shifts towards the higher angles, indicating that such a compound is located deeper than Y metal in each period. It is then located at the Y-on-B_4C interfaces. On the contrary, for sample 4, $[Pd/B_4C/Y]_{40}$, in Fig. 5(*d*), we have the angular shift of the compound curve towards lower angles. The compound is then located at a shallower depth than the Y metal, which should be the B_4C-on-Y interfaces. The unique appearance of such a compound at the Y–B_4C interfaces confirms our assumption of its nature: Y–B or Y–C. In the case of sample 2, $[B_4C/Pd/B_4C/Y]_{20}$, we have B_4C barrier layers on both sides of the Y layer. In Fig. 5(*b*), we observe an angular shift of the compound curve towards lower angles. This means that the formation of this kind of Y compound has a preference to occur, or is more active, at the B_4C-on-Y interfaces than at the Y-on-B_4C interfaces. Like the Pd $2p_{3/2}$ spectra, Y $2p_{3/2}$ spectra cannot provide us with information on whether there is any chemical compound formed at the Pd–Y interfaces because it is not possible to distinguish the alloy peak from the metal peak in the HAXPES spectra. The HAXPES–XSW curves of C $1s$ and B $1s$ (not presented) are very noisy due to the low
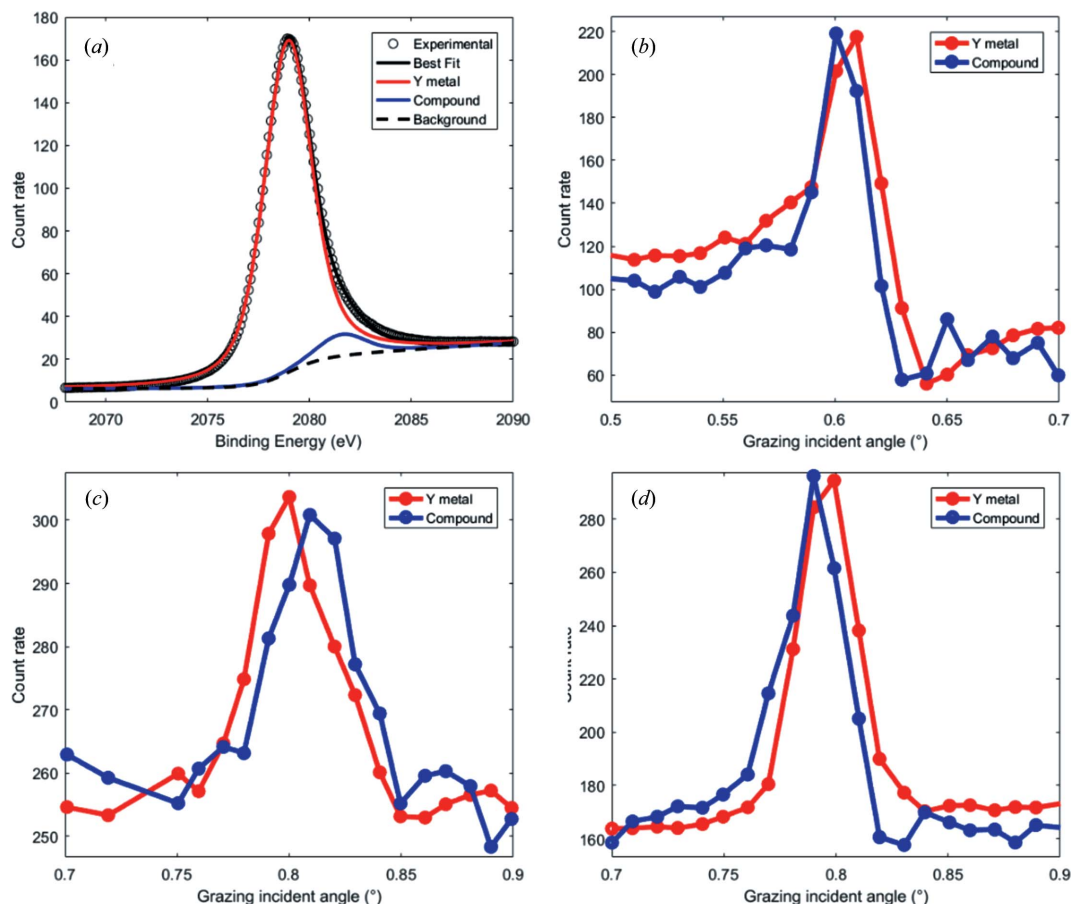
Figure 5
(a) Decomposition of the sum of all Y $2p_{3/2}$ photoemission spectra of sample 2. HAXPES–XSW curves of the corresponding component peaks of different samples, (b) sample 2, (c) sample 3, (d) sample 4.

intensity of their photoemission spectra. As a consequence, we cannot be sure whether the Y compound is Y–B or Y–C. The results obtained by HAXPES–XSW are in line with the values of enthalpy of formation ΔH_f found in the literature (Meschel & Kleppa, 2001).

The structural parameters in Table 1 determined by GIXR fitting are introduced into the software *YXRO* (Yang *et al.*, 2013) in order to calculate the variation of the photoemission intensity as a function of the grazing-incident angle. The calculation takes into account the complex refractive index of each material, the atomic cross section as well as the structure of the multilayer. The IMFP of the photoelectrons is calculated by *YXRO*. Such a prediction is presented in Fig. 6 for sample 2 where the HAXPES–XSW curves of the Pd $2p_{3/2}$, Y $2p_{3/2}$ and B $1s$ core levels are calculated with an angular range around the first-order Bragg angle. As seen in Fig. 1(b), when the grazing incident angle is at the Bragg angle (0.63° for sample 2), the anti-nodal planes of the periodic X-ray standing wave field are located at the Y-on-B$_4$C interfaces. Since both the multilayer and electric field are periodic with an identical period value, the same field distribution can be expected for each period of the stack with the progressive loss of amplitude due to the attenuation of the radiation. The oscillating structure on the HAXPES–XSW curves is centered close to the Bragg angle, because away from the Bragg angle the XSW
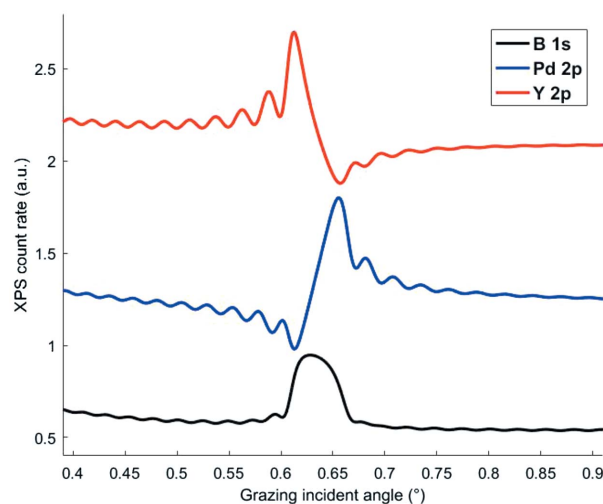

Figure 6
Simulation of the variation of the intensities of core-level peaks for sample 2: B $1s$ in black, Pd $2p_{3/2}$ in blue and Y $2p_{3/2}$ in red. The curves are vertically shifted for the sake of readability.

endures intensity loss due to the reflectance loss. When the incident angle varies through the Bragg angle, the location of the anti-nodal planes moves accordingly toward a deeper location from the Y layers into the B$_4$C layers and then the Pd layers. This angular order of the ionization enhancement of
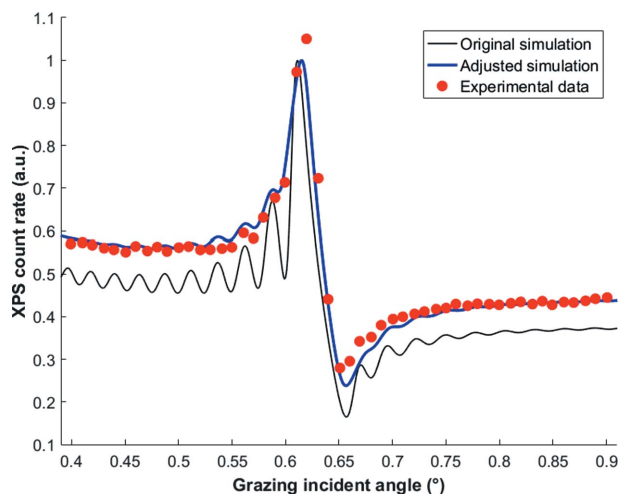
Figure 7
Comparison of the experimental (red dots) and calculated Y $2p_{3/2}$ HAXPES–XSW curves for sample 2 with (blue line) and without (black line) angular broadening.

the elements is reflected in Fig. 6. As the grazing angle varies from low to high values, a rise of the Y $2p_{3/2}$ HAXPES–XSW curve first appears at 0.61°. It is then followed by a rise of the B 1s and Pd $2p_{3/2}$ curves at 0.63° and 0.66°, respectively. As the B$_4$C layers are sandwiched between the Pd and Y layers, the B 1s HAXPES–XSW curve is rather more symmetrical instead of appearing as a 'Z' form like the Pd and Y curves.

Secondary oscillation of the calculated curves appears due to the interference between various reflections (so-called Kiessig fringes) resulting from the limited number of periods, *i.e.* 20 for sample 2. These simulations are far from what is experimentally observed (Fig. 5b). This discrepancy is overcome by taking into account the instrumental angular resolution (0.008°) and the horizontal divergence of the incident photon beam (0.026°). Such broadening can be mathematically simulated by applying a convolution by a gate function onto the simulation curve which is originally calculated with a step of 0.001°. The size of the gate function is then adjusted according to the angular resolution and beam divergence, and the effect is presented in Fig. 7 in the case of the Y $2p_{3/2}$ HAXPES–XSW curve. The Kiessig fringes disappear and the adjusted simulation shows a better agreement with the experimental data.
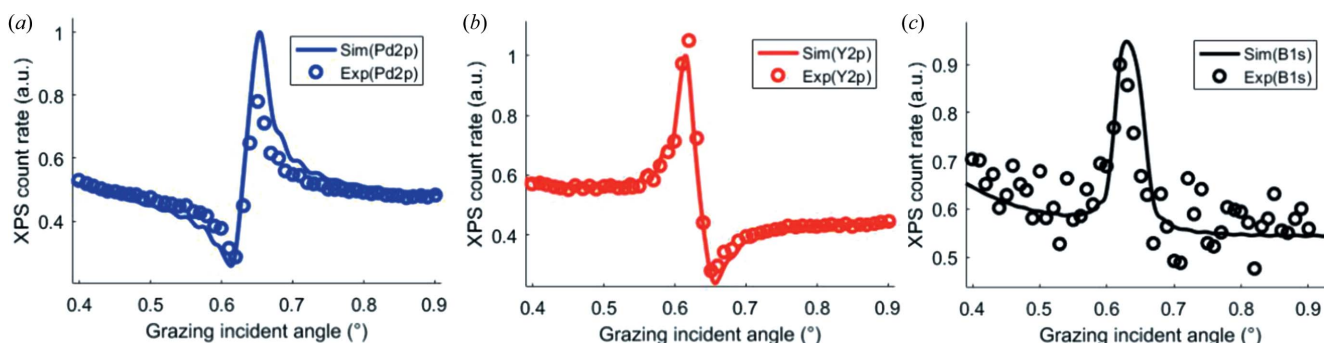
Fig. 8 presents the HAXPES–XSW curves related to the Pd 2p, Y 2p and B 1s peaks of sample 2 and their simulations with the broadening effect considered. The comparison shows a fine agreement indicating that the structure determined by GIXR is reliable as the shapes of these curves tightly correspond to the distribution of each element. For the other samples, the fitting of experimental curves based on the GIXR structural parameters is much less successful. The model used for GIXR fitting may be far too simple to describe the structure of the multilayer, especially concerning the depth distribution of all elements, even all chemical states. The reason for it working fine for sample 2 could be that the B$_4$C layers on each interface stabilize the multilayer by preventing the interdiffusion of Pd and Y atoms, making the situation relatively simple compared with other samples. The model used for the GIXR fitting of such a four-layer sample is thus suitable in this case. Unfortunately, for the moment we do not possess a fitting process to determine the structure of the multilayer independently.

4. Conclusion

The interdiffusion of the two metals in the Pd/Y system, predicted by calculating the mixing enthalpy using the Miedema model, is clearly seen in the GIXR spectrum of this sample. To study the efficiency of the insertion of a B$_4$C barrier layer at one or both interfaces, B$_4$C/Pd/Y, Pd/B$_4$C/Y and B$_4$C/Pd/B$_4$C/Y multilayers are also considered. The thickness and roughness/interdiffusion of the Pd and Y layers in these series are determined by fitting the experimental GIXR spectra. The interfaces are found to be asymmetrical since interdiffusion is stronger at Y-on-Pd interfaces than at Pd-on-Y interfaces.

The HAXPES–XSW measurements further help to explore the nature of the interdiffusion of Pd and Y. The interdiffusion of Pd into the B$_4$C layers does not form any chemical compound. On the contrary, Y forms chemical compounds with either B or C at the Y–B$_4$C interfaces. The formation of Y compound has a preference to happen, or is more active, at the B$_4$C-on-Y interfaces than at the Y-on-B$_4$C interfaces. Such chemical compounds can be the reason why the interfaces are stabilized.

Figure 8
Comparison of experimental and simulated HAXPES–XSW curves for sample 2. (a) Pd $2p_{3/2}$, (b) Y $2p_{3/2}$ and (c) B 1s.

Multiple HAXPES–XSW curves corresponding to different elements (or even different core levels of one element) are measured. A detailed description of the depth distribution of each element can be obtained by comparing the HAXPES–XSW curves with the calculations using *YXRO*. However, a fitting process, combining both XRR and HAXPES–XSW curves, is required in order to independently build up a model of the multilayer to determine its structure.

References

Bartel, T., Gaal, P., Reimann, K., Woerner, M. & Elsaesser, T. (2005). *Opt. Lett.* **30**, 2805–2807.

Campbell, J. L. & Papp, T. (2001). *At. Data Nucl. Data Tables*, **77**, 1–56.

Céolin, D., Ablett, J. M., Prieur, D., Moreno, T., Rueff, J.-P., Marchenko, T., Journel, L., Guillemin, R., Pilette, B., Marin, T. & Simon, M. (2013). *J. Electron Spectrosc. Relat. Phenom.* **190**, 188–192.

Fadley, C. S. (2013). *J. Electron Spectrosc. Relat. Phenom.* **190**, 165–179.

Fadley, C. S. (2016). *Hard X-ray Photoelectron Spectroscopy (HAXPES)*, Vol. 59 of *Springer Series in Surface Sciences*, edited by J. Woicik, pp. 1–34. Springer International Publishing.

Giglia, A., Mukherjee, S., Mahne, N., Nannarone, S., Jonnard, P., Le Guen, K., Yuan, Y.-Y., André, J.-M., Wang, Z.-S., Li, H.-C. & Zhu, J.-T. (2013). *Proc. SPIE*, **8777**, 87770I.

Kardellass, S., Selhaoui, N., Iddaoudi, A., Ait Amar, M., Karioui, R. & Bouirden, L. (2013). *MATEC Web Conf.* **5**, 04032.

Meschel, S. V. & Kleppa, O. J. (2001). *J. Alloys Compd.* **321**, 183–200.

Miedema, A. R., de Châtel, P. F. & de Boer, F. R. (1980). *Physica B + C*, **100**, 1–28.

Montcalm, C., Kearney, P. A., Slaughter, J. M., Sullivan, B. T., Chaker, M., Pépin, H. & Falco, C. M. (1996). *Appl. Opt.* **35**, 5134–5147.

Scofield, J. H. (1973). *Theoretical Photoionization Cross Sections from 1 to 1500 keV*. Technical Report UCRL-51326. California University, Livermore; Lawrence Livermore Laboratory, USA (doi:10.2172/4545040).

Shirley, D. A. (1972). *Phys. Rev. B*, **5**, 4709–4714.

Siervo, A. de, Landers, R., de Castro, S. G. C. & Kleiman, G. G. (1998). *J. Electron Spectrosc. Relat. Phenom.* **88–91**, 429–433.

Tu, Y.-C., Yuan, Y.-Y., Le Guen, K., André, J.-M., Zhu, J.-T., Wang, Z.-S., Bridou, F., Giglia, A. & Jonnard, P. (2015). *J. Synchrotron Rad.* **22**, 1419–1425.

Windt, D. L. (1998). *Comput. Phys.* **12**, 360.

Windt, D. L. & Gullikson, E. M. (2015). *Appl. Opt.* **54**, 5850–5860.

Wu, M., Burcklen, C., André, J.-M., Guen, K. L., Giglia, A., Koshmak, K., Nannarone, S., Bridou, F., Meltchakov, E., de Rossi, S., Delmotte, F. & Jonnard, P. (2017b). *Opt. Eng.* **56**, 117101.

Wu, M.-Y., Ilakovac, V., André, J.-M., Le Guen, K., Giglia, A., Rueff, J.-P., Huang, Q.-S., Wang, Z.-S. & Jonnard, P. (2017a). *Proc. SPIE*, **10235**, 102350F.

Xu, D., Huang, Q., Wang, Y., Li, P., Wen, M., Jonnard, P., Giglia, A., Kozhevnikov, I. V., Wang, K., Zhang, Z. & Wang, Z. (2015). *Opt. Express*, **23**, 33018–33026.

Yang, S.-H., Gray, A. X., Kaiser, A. M., Mun, B. S., Sell, B. C., Kortright, J. B. & Fadley, C. S. (2013). *J. Appl. Phys.* **113**, 073513.